On the wake deflection of vertical axis wind turbines by pitched blades

Huang, Ming; Sciacchitano, Andrea; Ferreira, Carlos

Important note
To cite this publication, please use the final published version (if applicable).
Please check the document version above.

WILEY

On the wake deflection of vertical axis wind turbines by pitched blades

Ming Huang ![ORCID] | Andrea Sciacchitano | Carlos Ferreira

Aerodynamics, Wind Energy, Flight Performance & Propulsion Department, Faculty of Aerospace Engineering, Delft University of Technology, Delft, The Netherlands

Correspondence
Ming Huang, Aerodynamics, Wind Energy, Flight Performance & Propulsion Department, Faculty of Aerospace Engineering, Delft University of Technology, Kluyverweg 1, 2629 HS Delft, The Netherlands.
Email: M.Huang-1@tudelft.nl

Abstract

Wake losses are a critical consideration in wind farm design. The ability to steer and deform wakes can result in increased wind farm power density and reduced energy costs and can be used to optimize wind farm designs. This study investigates the wake deflection of a vertical axis wind turbine (VAWT) experimentally, emphasizing the effect of different load distributions on the wake convection and mixing. A trailing vortex system responsible for the wake topology is hypothesized based on a simplified vorticity equation that describes the relationship between load distribution and its vortex generation; the proposed vorticity system and the resulting wake topology are experimentally validated in the wind tunnel via stereoscopic particle image velocimetry measurements of the flow field at several wake cross-sections. Variations in load distribution are accomplished by a set of fixed blade pitches. The experimental results not only validate the predicted vorticity system but also highlight the critical role of the streamwise vorticity component in the deflection and deformation of the wake, thus affecting the momentum and energy recoveries. The evaluation of the various loading cases demonstrates the significant effect of the wake deflection on the wind power available to a downwind turbine, even when the distance between the two turbines is only three diameters.

KEYWORDS

particle image velocimetry, vertical axis wind turbines, vortex dynamics, wakes

1 | INTRODUCTION

In wind farms, wake deflection is deemed an effective way to reduce the power loss of downwind wind turbines caused by the wake of upwind ones.[1] The deflection is often achieved by yawing the rotor discs of horizontal axis wind turbines (HAWTs), using an active control accounting for the variable wind direction.[2–7] With this technique, the wind farm's total power production is estimated to increase considerably, ranging from 4% to 13%, depending on specific cases.

Numerous investigations have been conducted on the wake deflection of HAWTs by yaw, both experimentally and numerically, highlighting the underlying physics and facilitating the development of analytical models.[8–14] Additionally, a recently proposed deflection technique via vertically tilting the rotor disc has earned attention, intending to increase the downdraft of high-momentum flow[15,16]; this approach enhances the vertical flux of kinetic energy, thus increasing the inflow velocity of downwind turbines and in turn improving the overall power output.[17,18] More recently, Bossuyt et al. (2021)[19] experimentally compared the wake deflections that occur in yawed and tilted HAWT and quantified the evolution

of counter-rotating vortices in the wake. With the support of those investigations, several time-efficient and accurate wake models that can retain the physics of the wake under yaw have been proposed.[13,14,20] Such models further facilitate the design of wind farms.

The wind farm design community has concluded that, to increase the overall power gain, one needs to focus on the power density of the wind farm as a whole, instead of the efficiency of individual turbines.[2,7,21] Increased power density has been investigated by redirecting/deflecting the wake or by modifying the wind farm layout (e.g., interturbine distance[22,23] and placement pattern[24]). As stated by those studies, wind farm power output can benefit from small sacrifices in the power output of upwind turbines that 'steer' the wake substantially around downwind turbines.

Vertical axis wind turbines (VAWTs) have a significant potential to achieve a higher power density than their counterparts in a wind farm. The main reasons are (a) faster wake recovery, allowing for a closer interturbine distance[25]; (b) less susceptible to flow turbulence, allowing for a more flexible layout to be deployed[26]; (c) in addition to the conventional aligned or staggered layout, synergistic clusters can increase farm efficiency[27]; and (d) simpler wake deflection mechanics. As opposed to yawed or tilted HAWTs that require the nacelle or tower to move, VAWTs can redirect the wake via pitched blades[28,29] or struts connecting the blades.[30]

The wake of VAWTs, on the other hand, is significantly more complex, and the physics underlying its deflection is still not fully understood. The characteristics of an isolated VAWT's wake have been extensively studied, with the majority of studies focusing on the topology (the outline of the shear layer, the strength and the three-dimensional distribution of the vortex structure, etc.)[31-34] or on the recovery of the wake.[25,35,36] There are also a few experimental studies on the analogy between the wakes of VAWTs and simpler objects, for example, circular cylinder[37,38] and rectangular meshes.[39,40] The importance of the vortex system in the wake of VAWTs has been highlighted. The vortex system consists of trailing vortices created around the blade tips, and spanwise vortices shed along the span of the blades. The trailing vortices form pairs of streamwise counter-rotating vortices that enhance the advection of momentum and are thus responsible for a faster recovery with respect to the wake of HAWTs; such vortex pairs are also responsible for the wake deformation. Additionally, shed vortices usually increase the turbulence intensity (TI) in the near wake, which in turn enhances the turbulent transport of energy.

However, an elaborate physical explanation of the wake deflection/asymmetry of a VAWT is still lacking. Some researchers associated it with the rotation of the rotor.[31,34] Many of them reported that the rotation of VAWTs creates two branches of horseshoe vortices similar to those of rotating cylinders,[31,38] and such vortex system causes the wake deflection.[25,33] In contrast, the results of De Tavernier et al[41] proved that a static cylindrical surface with three-dimensional loading can create counter-rotating vortices similar to a VAWT. The loaded cylindrical surface is the so-called three-dimensional actuator cylinder (AC) and is often used as a simplified VAWT. Massie et al. (2019)[42] simulated the wake behind an AC that applies the same time-averaged load distribution as a VAWT; the results verified the accuracy of this infinite-blade concept in reproducing vorticity and deflection and confirm that the fundamental cause of the deflection is related to the load distribution.

Therefore, it is likely viable to deflect the wake of VAWTs by varying the load distribution. Pitching the blades is the simplest way to modify the load. Ferreira (2009)[43] first proposed that by shifting the pitching axis of a VAWT, the blade load can be shifted upwind or downwind of the swept area of the rotor. Recently, LeBlanc and Ferreira (2021)[44] measured the blade load with an in-house designed VAWT that can perform active pitch control, showing that a fixed blade pitch can modify the blade load effectively. A few studies can also be found in the literature using the pitched blades on the deflection of VAWTs' wake. Jadeja (2018)[28] investigated the wake deflection of a pitched VAWT using the actuator line
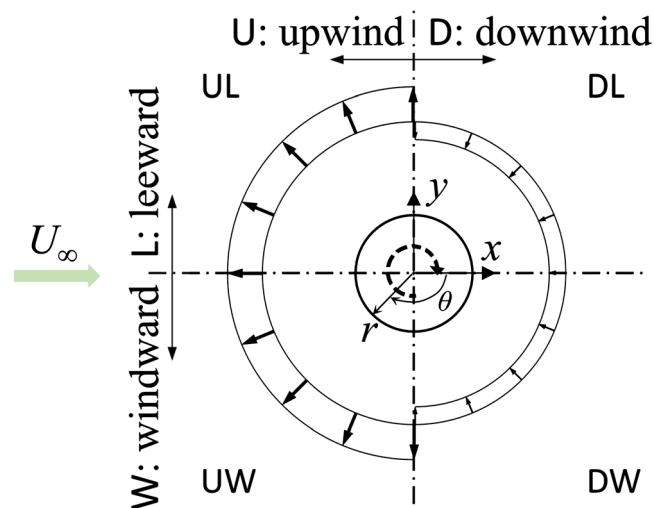

FIGURE 1 Top view of a simplified three-dimensional actuator cylinder, the AC is divided into four regions follows the convention of a clockwise rotating VAWT, with capital letters denoting corresponding quadrants (e.g., UW: upwind-windward) [Colour figure can be viewed at wileyonlinelibrary.com]

model together with unsteady Reynolds averaged Navier–Stokes (RANS) simulation. Based on the same numerical method, Guo and Lei (2020)[29] presents the deflected wake of a VAWT with inclined pitching axis.

The present work examines the wake deflection of VAWTs by pitched blades, emphasizing on the 3D loading effect. The load of the VAWT is modelled via the 3D AC model; the load distribution generates a vortex system that is responsible for the wake deflection. We performed stereoscopic particle image velocimetry (stereo-PIV) measurements in the wake of a lab-scale VAWT with different fixed-blade-pitch angles as a proof of concept. The measurements were taken between one and ten diameters behind the turbine, encompassing both the near and far wake regions. The results confirm that the streamwise vortex system is responsible for the majority of the macro-behavioural characteristics of a VAWT's wake, including the deflection and deformation of the wake's shear layer. We analyse the vortex system and the recovery of the VAWT's wake under various pitch conditions, demonstrating that the vortex system can be effectively manipulated by varying the fixed-blade-pitch angles of the blades. Additionally, the physics revealed in this work sheds light on the VAWT array's wake control strategy.

The remainder of the article is structured as follows. In Section 2, a theoretical analysis of the vortex system resulting from a 3D AC is provided, explaining the underlying physics that is responsible for the wake deflection of VAWTs; the theoretical analysis is followed by the descriptions of the experimental set-up and the data analysis procedures. Sections 3 and 4 present the results and key findings regarding the wake properties and the impact on VAWT arrays, respectively; Section 5 summarises the main conclusions of this work.

2 | METHODOLOGY

2.1 | Relation between the VAWT loading and the wake topology

The wake topology and its development is a direct consequence of the force field generated by a wind turbine, as expressed by the vorticity equation (see Appendix A1); different wake topologies will result in different wake deflections. Therefore, by understanding the relationship between the force field created by a VAWT and the wake topology it generates, we can interpret how force fields affect wake deflections. In this section, we use the 3D AC model as an idealization of a VAWT and apply the vorticity transport equation to understand the relation between the force field of a VAWT and the resulting wake topology. We discuss how certain load distributions generate trailing vortices and how these vortices affect the wake topology and deflection, under the induced velocity concept.[45]

2.1.1 | Three-dimensional AC

Here, we introduce the idealization of a VAWT based on the three-dimensional AC model, which has been verified as a good representation of an H-type VAWT.[42] The AC has a height-to-diameter ratio of one, the same as the VAWTs investigated in the literature (e.g., Tescione et al[34] and LeBlanc and Ferreira[44]). For simplicity, assume the load is uniformly distributed in the upwind and downwind locations, respectively, with the upwind half loaded more heavily (Figure 1). The latter is also the case for most H-type VAWTs with zero blade pitch in the literature (e.g., Massie et al[42] and Madsen et al.[46]); all the force vectors are perpendicular to the cylindrical surface, based on the previous observation that normal loading accounts for most of the total turbine loading.[47] Moreover, the force vectors point to upwind, assuming that the loading from each region consumes/extracts streamwise kinetic energy of the inflow. The AC is divided into four quadrants as illustrated in Figure 1, marked with UL, DL, DW and UW, respectively. The division follows the convention of a VAWT rotating clockwise. It is noted that the AC is static, and such division is only for the ease of discussion hereafter.

2.1.2 | Vorticity generation by the AC

We introduce here the principle of vorticity generation of ACs. The simplified vorticity equation for incompressible and inviscid flow is given by

$$\rho \frac{D\boldsymbol{\omega}}{Dt} = \nabla \times \mathbf{f},\tag{1}$$

where ρ is the air density and $\boldsymbol{\omega}$ and $\mathbf{f}$ are vorticity vector and body force vector, respectively. The equation holds for a VAWT for two reasons: (a) due to the low Mach number, a flow field wherein a wind turbine is placed can be regarded as incompressible; (b) the viscous terms can be neglected due to a sufficiently large diameter-based Reynolds number. However, this equation is only valid for the vorticity generation; if the vortex evolution needs to be resolved, the vortex stretching terms should be retained. More details about the derivation of Equation (1) is provided in Appendix A1.
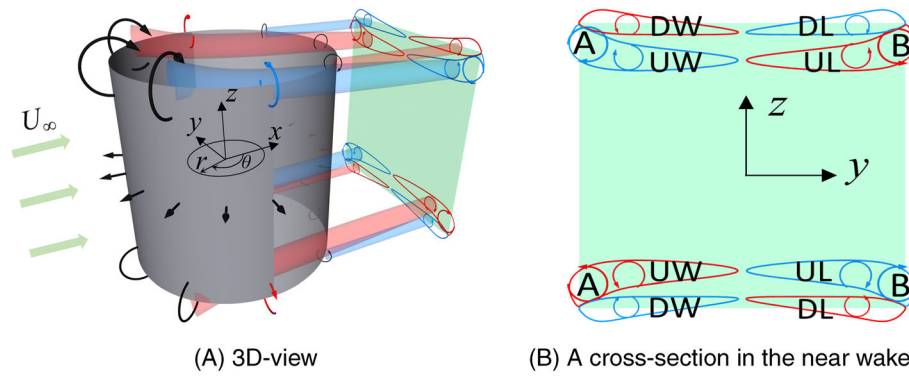
FIGURE 2 Schematic of the trailing vortex system generated by an actuator cylinder. (A) 3D view. Curled arrows in black: trailing vortices; arrows in red and blue: streamwise components of the trailing vortices with positive and negative vorticity values, respectively. Tubular shade in red and blue: propagation paths of some of the streamwise vorticity. (B) A cross-section in the wake. A and B: two pairs of counter-rotating vortices with the largest streamwise vorticity on the windward and leeward side, respectively. Closed red and blue curves: regions with nonzero vorticity; capital letters ('UW' and so on): the generation region of the vorticity, corresponding to the division in Figure 1. Green square: the frontal area of the AC [Colour figure can be viewed at wileyonlinelibrary.com]

Now, we apply the principle to the three-dimensional AC. Rewriting Equation (1) in cylindrical coordinates, and eliminating the terms with zero value ($f_\theta = f_z = 0$), one obtains

$$
\rho \frac{D\boldsymbol{\omega}}{Dt} = \nabla \times \mathbf{f} = \frac{1}{r} \begin{vmatrix} \hat{e}_r & r\hat{e}_\theta & \hat{e}_z \\ \frac{\partial}{\partial r} & \frac{\partial}{\partial \theta} & \frac{\partial}{\partial z} \\ f_r & rf_\theta & f_z \end{vmatrix} = \frac{1}{r} \left[\left(\frac{\partial f_z}{\partial \theta} - \frac{\partial (rf_\theta)}{\partial z} \right) \left(-\frac{\partial f_z}{\partial r} + \frac{\partial f_r}{\partial z} \right) \left(\frac{\partial (rf_\theta)}{\partial r} - \frac{\partial f_r}{\partial \theta} \right) \right] \begin{bmatrix} \hat{e}_r \\ r\hat{e}_\theta \\ \hat{e}_z \end{bmatrix}
$$

$$
= \begin{cases} \dfrac{\partial f_r}{\partial z} \hat{e}_\theta, & \text{when } r = \dfrac{D}{2}, z = \pm \dfrac{H}{2} \\[2mm] \dfrac{\partial f_r}{\partial z} \hat{e}_\theta - \dfrac{1}{r} \dfrac{\partial f_r}{\partial \theta} \hat{e}_z, & \text{when } r = \dfrac{D}{2}, |z| \leq \pm \dfrac{H}{2}, \text{ and } \theta = 90° \text{ or } 270°, \end{cases}
$$

(2)

where $\hat{e}_r$, $r\hat{e}_\theta$ and $\hat{e}_z$ are the unit vectors for the r, θ and z axes, respectively.

Equation (2) reveals that the vorticity is mostly generated along the top and bottom edges of the AC, except for the spanwise vorticity generated along the connections of the upwind and downwind half of the AC. An overview of resulting trailing vortex system is illustrated schematically in Figure 2A, with the black curled vectors denoting the trailing vortices, red and blue vectors are the streamwise vorticity components pointing to the positive and negative x axis, respectively. The spanwise vorticity is not presented. The propagation paths of some of the streamwise vorticity are shaded.

For the upwind half of the AC, vortices along the periphery of the cylinder induce an inboard velocity component on the top and bottom lids of the cylinder. On the contrary, the downwind part produces the opposite, with the vortices creating an outboard velocity component. Therefore, the upwind trailing vortices are transported more to the centre plane ($z/D = 0$) compared to downwind ones, as illustrated with the shaded paths in Figure 2A. In Figure 2B, a cross-section in the near wake is presented, where only streamwise vortices are presented. This is because the streamwise vorticity is deemed to be the most important factor related to the wake deflection and deformation.[25] In the cross-section, the green square is the frontal area of the AC. The vortices marked with A and B are the strongest streamwise counter-rotating vortex pairs (CVPs) appear in the windward and leeward of the wake, respectively. Closed curves that are marked with capital letters represent the region with nonzero streamwise vorticity: red for the positive and blue for negative. The capital letters are for different quadrants shown in Figure 1, denoting the generation region of the vorticity. Such streamwise vortex system is verified in Section 3.4.

2.1.3 | Wake deflection incurred by the streamwise vorticity

To understand the pattern of wake deflections, we further simplify the hypothesized streamwise vorticity system proposed in Section 2.1.2, based on the previous simulation results on the wake topology of ACs.[41] The simplification is illustrated in Figure 3. The strongest vortex pairs A and B at windward and leeward sides are illustrated as they are deemed the primary reason for the wake deflection and deformation. In contrast,
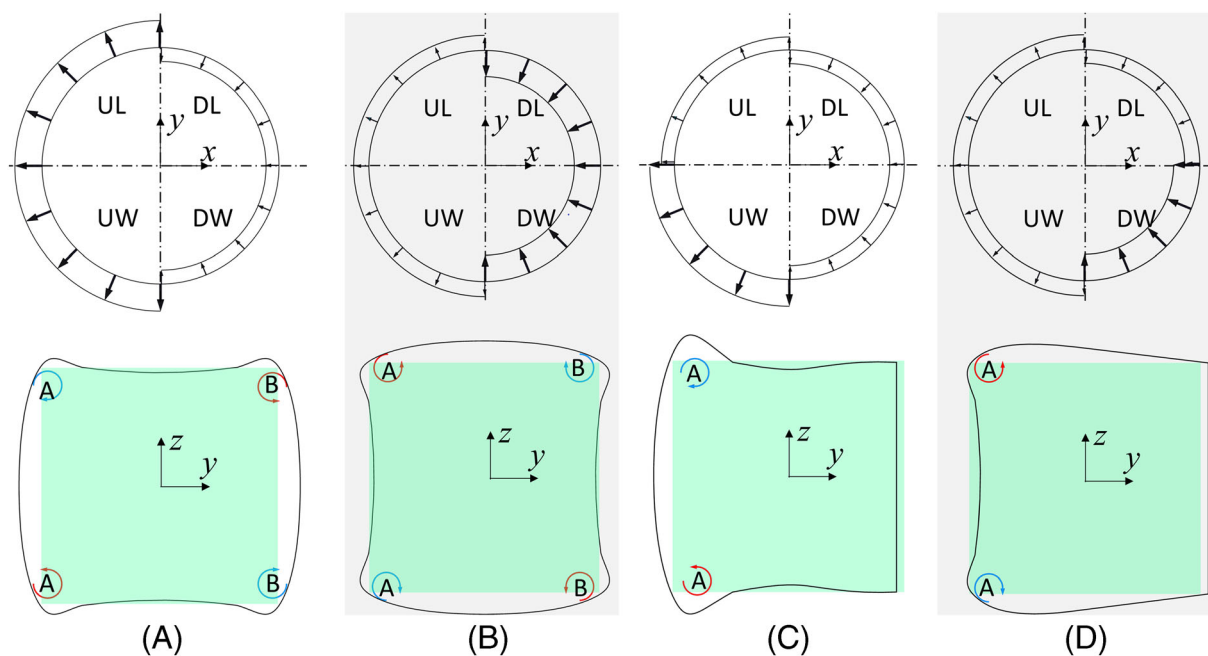
FIGURE 3 Schematic of wake deflections caused by 3D actuator cylinders with different force fields. The first row shows the force fields and the second row consists of the resuting wake topologies. The incoming flow direction and the coordinate system follows those in (A), with green square denoting the frontal area of the AC, and the black lines for the wake outline. (A,B) The ACs are loaded equally windward and leeward but loaded more heavily upwind or downwind, respectively; (C,D) the ACs are loaded more at UW and DW regions, respectively [Colour figure can be viewed at wileyonlinelibrary.com]

double-layer vorticity regions (closed curves in Figure 2B) are neglected, under the assumption that vortices at those regions will eventually merge with the stronger vortices A and B in the far wake.

Four ideal force fields are presented in Figure 3 to demonstrate the concept. The initial wake shape is assumed to be a square that is the same as the frontal area of the AC. The wake is deformed under the velocity induced by the streamwise vorticity; the wake shapes after deformation is depicted with the closed black curves.

When the resulting lateral force is null (Figure 3A,B), wake deforms but does not experience a lateral deflection. With the upwind half loaded more, the wake expands more horizontally. In contrast, when the downwind half is loaded more, the wake is stretched vertically. On the other hand, wake deflections occur when the resulting lateral force is not null. For example, applying more load in the UW region as depicted in Figure 3C will increase the strength of the CVP-A, resulting in a wake deflection towards the windward side. On the leeward side, the vorticity generated from upwind and downwind has the same magnitude and the opposite direction, thus in first approximation the generated streamwise vortices cancel out. Conversely, when the DW region is loaded more than the other regions, the wake deflects towards the leeward side, as illustrated in Figure 3D.

In all, the wake deflection of an AC (a simplified VAWT) is due to an overall lateral force and is accompanied by a deformation which is closely related to the dominating CVPs appearing in the wake. It is worth to mention that the four cases in Figure 3 are extremely simplified; for a VAWT under more realistic working conditions (e.g., dynamic inflow, dynamic stall, etc.), the wake topology will be more complicated, with the location and strength of CVP-A and CVP-B varying. Nonetheless, those complex configurations can be described with combinations of the four cases above, and this is verified with the experimental results presented in Section 3.4.

2.2 | Experimental set-up

2.2.1 | Wind tunnel facility and VAWT model

The experiments are conducted in the Open-Jet Facility (OJF) of the TU Delft Aerospace Engineering Laboratories. The OJF features an open exit of 2.85 m $\times$ 2.85 m and a TI lower then 2% within the test region at the free-stream velocity of $U_\infty = 5\,\mathrm{ms}^{-1}$ (see Lignarolo et al.[48]). The uniform-flow region reduces to $2 \times 2\,\mathrm{m}^2$ at 6 m (20D) from the jet exit, which covers the entire area of interest even for the case with significant wake deflection (P10 as introduced in Section 2.2.5).
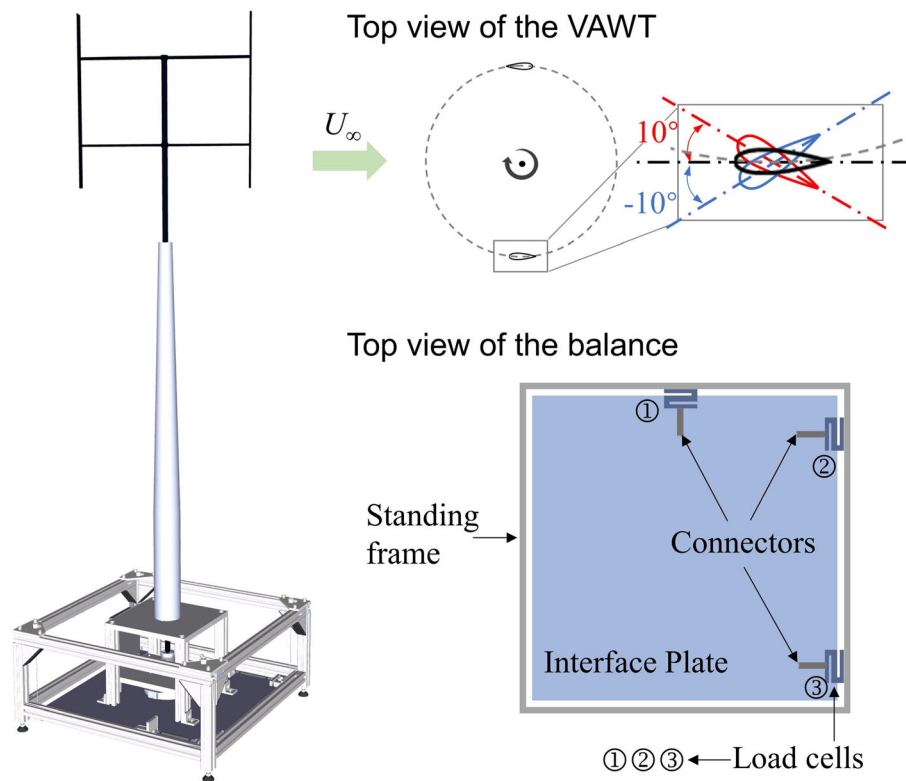
FIGURE 4 Schematic of the tested VAWT model mounted on the in-house designed balance [Colour figure can be viewed at wileyonlinelibrary.com]

TABLE 1 Attributes of the VAWT model

Symbol	Parameter	Value
N_s	Number of struts	4
B	Number of blades	2
D	Rotor diameter (m)	0.3
c	Chord length (m)	0.03
D_t	Tower diameter (m)	0.01

The tested VAWT is an H-type, with a rotor size of 30 cm × 30 cm. The resulting Reynolds number based on the diameter is about 1.0×10^5. The tip speed ratio $\lambda = u_t/U$ is fixed to 2.5 to keep a moderate thrust coefficient and a comparable working condition for all the cases studied, where u_t denotes the linear speed of the blades. The pitch conditions are illustrated in Figure 4. The attributes of the VAWT are listed in Table 1, while a sketch of the device can be seen in Figure 4. It is noted that no ground effect is considered in the experiment.

2.2.2 | Load measurement

A three component balance that is in-house designed and constructed is employed for the load measurement, enabling a quantification of both the drag (equals to the VAWT's thrust) and the lateral force.

The balance consists of three S-shape load cells (type: KD40s, max range ±50 N, max error ⩽0.1%), with two of them measuring the streamwise force (drag/thrust) while the other one measuring the lateral force. These load cells are mounted on the bottom part of the same standing frame that is stiff enough to avoid severe vibration and deformation. The other ends of the load cells are connected to the interface plate, on which the VAWT is mounted, using specially designed connectors. Those special connectors are flexural rods that transmit forces only along their spanwise, delivering no moment. They make sure the load cells measure only the tensile or compressive forces (no shear forces are

applied). The interface plate is lifted with four steel strings; together with the load cells, they allow for minor structural deformation in the directions of the flexural rods while preventing rotations caused by the torque (Figure 4). When the flexural rods are aligned with streamwise and lateral forces respectively, the overall uncertainty of the force measurement is of the same level as the load cells.

Compared with the previous balance system proposed in Huang et al,[40] the current design forms a cantilever system so that all the horizontal forces applied to the VAWT will be balanced and thus measured by the load cells, yielding more accurate measurements.

2.2.3 | Stereoscopic particle image velocimetry

A stereoscopic particle image velocimetry set-up is used to measure the velocity fields in cross-sections of the VAWT's wake. A SAFEX smoke generator releases water-glycol seeding particles of average 1 μm diameter. A Quantel *Evergreen* double-pulsed Nd:YAG laser produces pulses with 200 mJ energy at a wavelength of 532 nm within a laser sheet of approximately 3 mm thickness. The seeding particles are imaged by two LaVision's Imager sCMOS cameras in successive cross-sections of the wake. In doing so, a traversing system is employed whereby the stereo-PIV set-up is mounted, enabling navigation from 1 to 10 diameters (D) downstream with a step of $1D$. An overview of the experiment set-up is shown in Figure 5; with the illustrated set-up, a field of view (FoV) of approximate 80×55 cm^2 is achieved. More technical specifications are listed in Table 2.

2.2.4 | Uncertainty of the flow field measurement

Following the work of Sciacchitano and Wieneke,[49] we introduce the uncertainties of relevant quantities here. This work deals with the time-averaged velocity, of which the standard uncertainty can be calculated as

$$U_{\bar{U}} = \frac{\sigma_U}{\sqrt{N}},$$

(3)

where σ_U is the standard deviation of the velocity U, which has three components u, v and w, respectively. For its streamwise component (the out-of-plane velocity), σ_u reaches its highest value typically at the shear layer, not exceeding 0.6 ms. The effective number of samples N is around 400, resulting in uncertainty values below 0.03 ms (less than 1% of local velocity) in the shear layer. For the in-plane velocity components (v and w), smaller standard deviations in the shear layer around 0.4 ms are obtained. Following Equation (3), the maximum value of $U_{\bar{v}}$ or $U_{\bar{w}}$ is 0.02 ms.

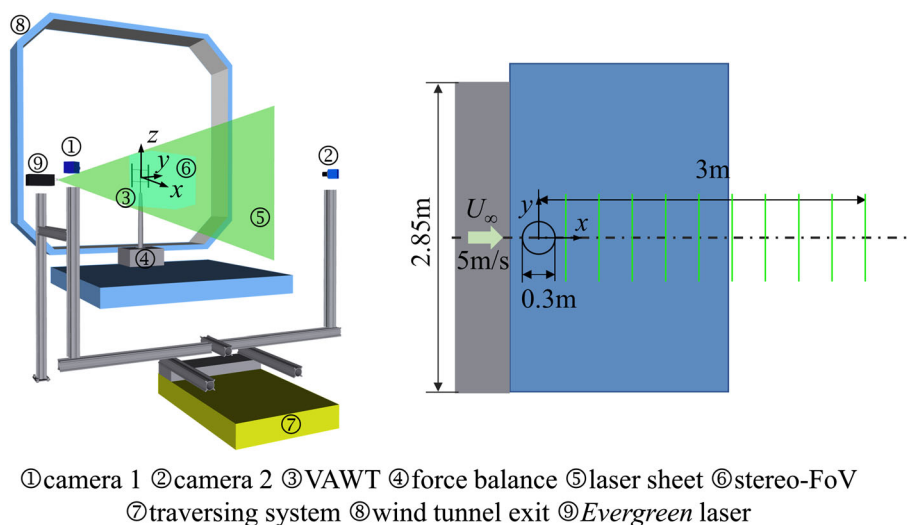The uncertainty of the time-averaged out-of-plane (i.e., streamwise) vorticity is formulated as

①camera 1 ②camera 2 ③VAWT ④force balance ⑤laser sheet ⑥stereo-FoV
⑦traversing system ⑧wind tunnel exit ⑨*Evergreen* laser

FIGURE 5 Left: Schematic of the experimental set-up with the equipment labelled. The origin of the coordinate system is placed at the centre of the rotor. Right: A sketch of the top view presenting the size of the set-up and the PIV acquisition locations [Colour figure can be viewed at wileyonlinelibrary.com]

TABLE 2 Technical specifications of the stereo-PIV set-up

Seeding	Tracer particle	Water-glycol particles
	Particle size	1 μm
	Particle density	10^3 kg m^{-3}
Illumination	Pulse energy	2×200 mJ
	Wavelength	532 nm
	FoV	Approx. 800×550 mm^2
Imaging	Active sensor	2560 px $\times$ 2160 px
	Pixel pitch	6.5 μm
	Acquisition frequency	15 Hz
	Δt	230 μs
Optics	Focal length	50 mm
	Numerical aperture	4
Data processing	Interrogation window size	32 px $\times$ 32 px (8.22×8.22 mm^2)
	Overlap factor	75%
	Vector pitch	2.055 mm

$$U_{\overline{\omega_x}} = \frac{U_{\overline{\text{vor}\overline{w}}}}{d} \sqrt{1 - \rho(2d)}, \tag{4}$$

where $U_{\overline{\text{vor}\overline{w}}}$ is the uncertainty of time-averaged in-plane velocity vectors. d and $\rho(2d)$ denote grid spacing of the interrogation window and cross-correlation coefficient of spatially correlated velocities, respectively. As listed in Table 2, $d = 8.22$ mm. For the interrogation window size and overlap factor adopted in the present work (see Table 2), $\rho(2d) \cong 0.45$.[49] Hence, the value of $U_{\overline{\omega_x}}$ is lower than 1.81 s^{-1}.

The uncertainty of the Reynolds normal stress is given by

$$U_{R_{uu}} = \sigma_u^2 \sqrt{\frac{2}{N-1}} \leqslant 0.025 \, \text{m}^2 \, \text{s}^{-2}. \tag{5}$$

Similarly,

$$U_{R_{vv}} = U_{R_{ww}} \leqslant 0.006 \, \text{m}^2 \, \text{s}^{-2}. \tag{6}$$

Furthermore, the uncertainty of the turbulence kinetic energy $\left(\text{TKE} = \frac{1}{2} \overline{u_i' u_i'} = \frac{1}{2}(R_{uu} + R_{vv} + R_{ww}) \right)$ is expressed as

$$U_{\text{TKE}} = \frac{1}{2} \sqrt{U_{R_{uu}}^2 + U_{R_{vv}}^2 + U_{R_{ww}}^2} \leqslant 0.014 \, \text{m}^2 \, \text{s}^{-2}. \tag{7}$$

2.2.5 | Cases description

In order to modify the load distribution of the VAWT, and investigate the effect of fixed blade pitch on the wake development, three cases with $-10°$, $0°$, and $10°$ pitch angles are selected. The convention of the sign of the pitch angles is indicated in Figure 4, with the blade pitching towards the rotating axis as positive. For simplicity, the cases are numbered in Table 3. It is worth noting that these extreme pitch angles were chosen to emphasize the pitched blade's significant effect on wake deflection. The quantitative effect of these pitch angles on dynamic stall is beyond the scope of this work. However, here we qualitatively discuss where dynamic stall occurs in different pitch cases and how it yields different loading over the swept area of VAWT blades. In doing so, we calculate the blade's angle of attack (α) while rotation using the 2D AC model proposed by Madsen (1983).[50] For simplicity, the lift-drag polar of a flat plate is adopted, without dynamic stall correction. The results, as illustrated in Figure 6, indicate the dynamic stall regions, where exceedingly high $|\alpha|$ is perceived. For instance, for P10 case, the blades operate above the static stall angle within the upwind half of the rotor, while the most severe flow separation and aerodynamic force drop likely occur in the upwind-leeward region ($\theta \approx 100°$). On the contrary, P-10 would feature dynamic stall at the downwind rotor.

TABLE 3 Configurations

Case	Description
P-10	With pitched blades, $-10°$
P0	Zero-pitch angle
P10	With pitched blades, $+10°$
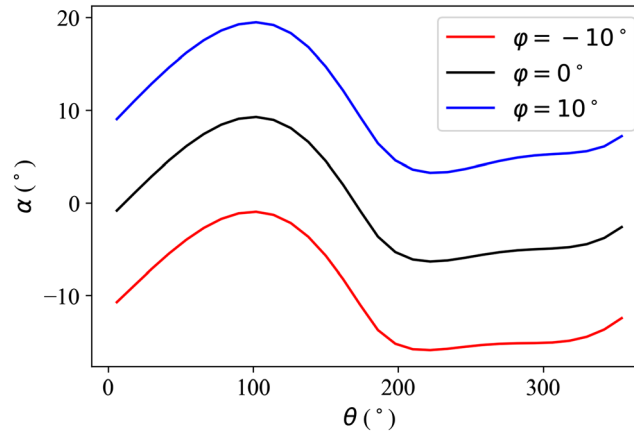
FIGURE 6 A schematic of blade-pitch effect on the angle of attack variation. φ: the angle of fixed blade pitch [Colour figure can be viewed at wileyonlinelibrary.com]

2.3 | Wake analysis procedures

2.3.1 | Wake centre

To compare the deflections quantitatively, the wake centre is calculated with a 'centre of mass' method with respect to the velocity deficit; this method is widely accepted in characterizing the wake topology of wind turbines[31,51]:

$$y_c(x) = \frac{\iint y \Delta \bar{u}(x,y,z) \mathrm{d}y \mathrm{d}z}{\iint \Delta \bar{u}(x,y,z) \mathrm{d}y \mathrm{d}z}, \tag{8}$$

where $\Delta \bar{u}(x,y,z) = U - \bar{u}(x,y,z)$. The integrals are computed over cross-sectional planes, perpendicular to the streamwise velocity. Only the horizontal coordinate of the wake centre is discussed in this article, since the pitched blades mainly yield lateral deflection of the wake.

2.3.2 | Streamwise momentum budgets

The RANS equation is rearranged as Equation (9) to inspect the budget of streamwise momentum. This process is widely adopted to identify the main contributors to the momentum recovery,[19,36] the latter is critical in a wind farm. In Equation (9), the viscous terms are neglected due to the sufficiently high Reynolds number in the wake (1×10^5, based on the rotor diameter):

$$\underbrace{\bar{u}\frac{\partial \bar{u}}{\partial x}}_{} = \underbrace{-\bar{v}\frac{\partial \bar{u}}{\partial y} - \bar{w}\frac{\partial \bar{u}}{\partial z}}_{\text{advection}} \underbrace{-\frac{1}{\rho}\frac{\partial \bar{p}}{\partial x}}_{\text{pressure}} \underbrace{-\frac{\partial \overline{u'u'}}{\partial x} - \frac{\partial \overline{u'v'}}{\partial y} - \frac{\partial \overline{u'w'}}{\partial z}}_{\text{Reynolds stress}}, \tag{9}$$

where u, v and w represents streamwise (x), transverse (y) and vertical (z) velocities, respectively; p is pressure; and ρ is density. Overlines stand for time-averaging and primes for fluctuations.

The equation is constituted by three parts, that is, the advection terms, the pressure term and the Reynolds stress terms. Except for the streamwise advection term $\bar{u}(\partial \bar{u}/\partial x)$, the remaining terms are written to the right-hand side (RHS) to examine their contributions to the streamwise momentum recovery.
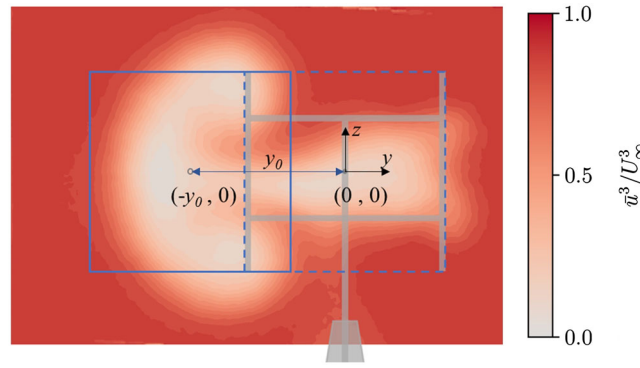
FIGURE 7 Schematic of the integration window for AP estimation. Square with solid blue line: integration window moving transversely; dashed square: frontal area of the VAWT; background contour: the normalized streamwise wind power, $\bar{u}^3/U^3$ [Colour figure can be viewed at wileyonlinelibrary.com]

2.3.3 | Available power (AP)

Different momentum recovery will cause different AP distribuion in the wake. To visualize the impact of the wake deflection on the available wind power (AP) distribution under different pitched blade conditions, and identify the best location for a downwind wind turbine in array configurations, a moving average of the coefficient of available streamwise wind power ($\bar{u}^3/U^3$) within the frontal area of a hypothetical downwind VAWT is presented in Section 4.3. The calculation is formulated as

$$\begin{cases} f_{AP}(x_0, \ y_0, \ z_0) = \int \int_S \bar{u}^3(x_0, \ y, \ z)/U^3 dz dy/(DH) \\ \qquad S: |y - y_0| \leqslant 0.5D, \ |z| \leqslant 0.5H \end{cases}, \tag{10}$$

where f_{AP} represents the coefficient of AP. (x_0, y_0, z_0) is the coordinate of the centre of the hypothetical downwind VAWT. D and H are the diameter and the height of the VAWT. The hypothetical VAWT has the same dimension as the pitched (upwind) VAWT. The integration and average is performed within a translating square with the same area as that of the VAWT. A schematic of the integration window and its coordinate system is depicted in Figure 7: At a given cross-section ($x = x_0$) downstream of the upwind VAWT, the solid blue box is the current integration window, while the dashed one is the projection of the upstream turbine. The coordinate system, specifically the horizontal axis y for Figure 7, is defined as follows: The origin is the centre of the dashed box, y is positive towards the right. The contour in the background represents the integrated quantity, in this case is the normalized streamwise wind power, $\bar{u}^3/U^3$.

A theoretical comparison of f_{AP} based on the classical actuator disc (AD) theory is provided as well. The AD model is extremely simplified in that only considers the streamwise momentum conservation, whereas no recovery and no deflection is accounted for in the model. The AD model is well accepted for estimating the maximum velocity deficit and minimum f_{AP} in the near wake of a wind turbine. It has been adopted in the most advanced engineering wake models.[1,17] The model takes the streamwise thrust coefficient $C_{T,x}$ as input, calculating the induction factor $a = (1 - \sqrt{1 - C_{T,x}})/2$, and further the minimum wake velocity $u_w = (1 - 2a)U$. In this way, the minimum coefficient of AP for a hypothetical downwind wind turbine that is inline with the upwind one can be estimated as

$$f_{AP|AD} = \bar{u}_w^3/U^3 = (1 - C_{T,x})^{3/2}. \tag{11}$$

3 | RESULTS AND DISCUSSION

3.1 | Thrust and lateral force

The streamwise and lateral thrusts ($C_{T,x}$ and $C_{T,y}$) are given by

$$C_T = \frac{T}{0.5 \rho U_\infty^2 A}, \tag{12}$$

where T is the measured thrust, equivalent to the force perceived by the turbine. $A = DH$ is the frontal area of the turbine. As it can be seen in the results of Table 4, the negative pitched angle slightly decreases the thrust and the lateral force, compared to the zero-pitch case. This is caused by

TABLE 4 Measured $C_{T,x}$ and $C_{T,y}$

Case	$C_{T,x}$	$C_{T,y}$
P-10	0.60	0.09
P0	0.65	0.14
P10	0.81	0.39

two factors: (a) the blades work in a decreased angle of attack during the upwind pass and (b) deep stall occurs on the downwind pass. These factors result in a decreased blade loading along the revolution passage, and therefore, an overall decreased thrust and lateral force. Such phenomenon has been confirmed by both load and flow field measurements performed on the blades of a larger H-type VAWT.[44] In contrast, positive pitch increases both streamwise and lateral force by 25% and 180%, respectively. Besides that, LeBlanc and Ferreira (2021)[44] reported significantly increased blade load in the upwind-windward region, and a sudden drop in the upwind-leeward region. The same happens in the current measurement, which can be justified by the averaged velocity deficit fields presented in Section 4.1. That is, P10 features a deeper momentum deficit in the windward side compared with P0, while less deficit in the leeward side.

3.2 | Velocity fields

The measured time-averaged streamwise velocity contour and in-plane velocity vectors are presented in Figure 8. The velocities are normalized with the free-stream velocity U. The wake of P-10 features a minimum streamwise velocity around $0.3U$. The outline of the wake cross-section in the near wake region $(x/D = 1)$ is a square that is elongated along its vertical symmetric axis. The elongation lasts to the far wake.

The case with zero pitch, P0, features a similar maximum velocity deficit and a slightly larger wake deflection compared to P-10 based on the visual comparison of the contour colour. The similarity between the two wakes is attributed to the similar streamwise and lateral thrust exerted by the turbine, which can be justified by the load measurement results listed in Table 4. However, large discrepancies in terms of the cross-sectional shapes of the wake between these two cases are observed. The outline of P0's wake cross-section is formed into a trapezoid at $x/D = 1$ instead of the stretched square for P-10. The difference of the wake outlines is attributed to distinct streamwise vorticity distributions, which are further discussed in Section 3.3.

In contrast, the wake of P10 presents a remarkable lateral deflection towards windward and a cross-sectional deformation as predicted in Figure 3C. Guo and Lei (2020)[29] reported similar cross-sectional shapes using RANS simulation integrated with the actuator line model. Besides, P10 features a larger wake region and a deeper velocity deficit in the proximity of the turbine, which are ascribed to stronger lift produced by the advancing blades at windward side, resulting in a larger side force inducing lateral velocities. A similar phenomenon has been documented in the literature (see previous studies[25,33,40]).

3.3 | Streamwise vorticity

An overview of the normalized streamwise vorticity fields is presented in Figure 9. The streamwise vorticity plays a key role in forming the wake shape until at least $5D$ downstream of the VAWT model and is still noticeable at $x/D = 10$. The vorticity is normalized with $C_{T,x}U/D$. While normalization for vorticity using U/D is well accepted in the literature,[25,31] the values of $C_{T,x}$ are also used in the current study to compensate the effect of different loading level. The use of the thrust coefficient in the normalization of the vorticity is chosen because the wake deflection is analysed in relation to the deflection of thrust vectors, and the vorticity generated remains proportional to both the cross-flow component and the balance between upwind and downwind loading. For vectors with different magnitudes, the overall lateral force can be the same, so as the wake deflection. However, the local vorticity magnitude will be completely different. To avoid such deviation and make the vorticity magnitude consistent with the deflection, the force magnitude should be taken into account for normalization. And we select the the main component, the streamwise thrust coefficient, for simplicity.

The streamwise vorticity is mainly produced by the trailing vortices that are generated at the blade tips according to Helmholtz's theorem.[31,33] By pitching the blade, the blade load along its rotation passage is modified, so is the vortex system. As discussed in Section 3.2, P-10 and P0 feature largely different wake shapes as they possess different blade loads, although the integrated thrusts are similar. P10 features two pairs of strong counter-rotating vortices at windward and leeward, respectively.

3.4 | Verification of the hypothesized vorticity system

We compare the measurement results with the vorticity system proposed in Section 2.1 by identifying the components illustrated in Figure 2B. The normalized streamwise vorticity fields at $x/D = 1,3,5$ are presented in contour plots in Figure 10, together with the in-plane streamlines that
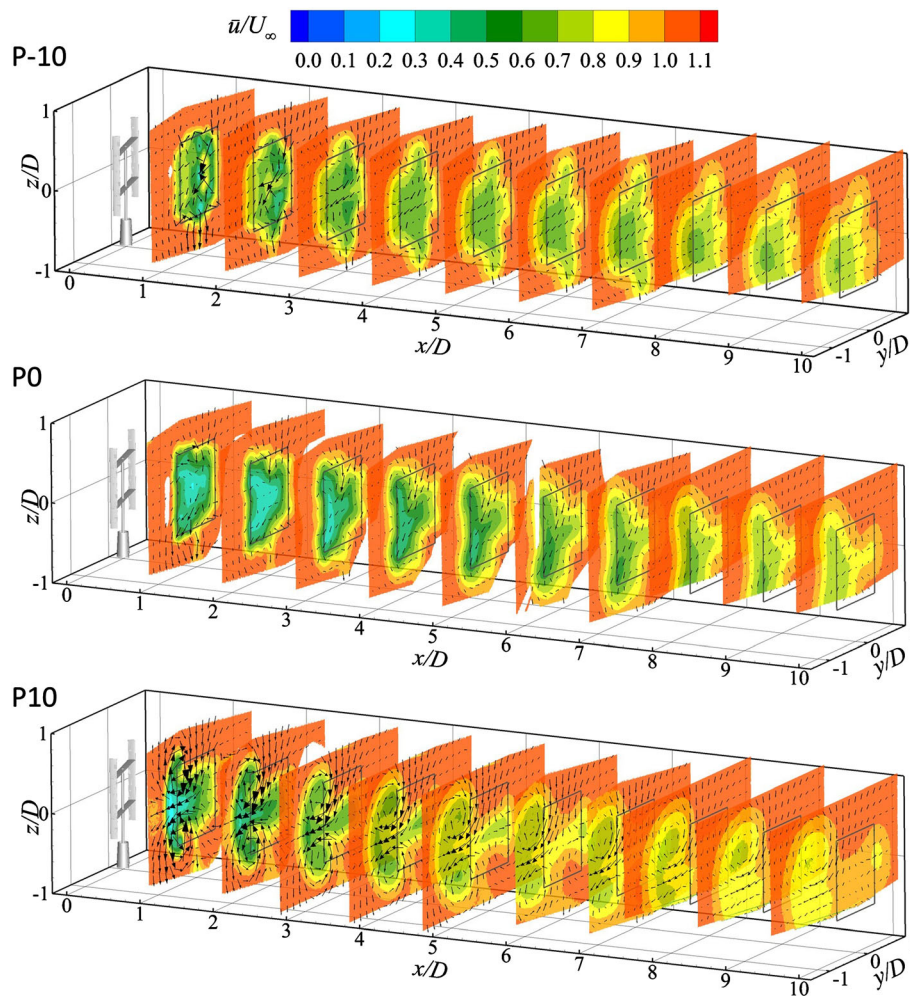
FIGURE 8 Contours of normalized streamwise velocity with in-plane velocity vectors from 1 to 10 D after the VAWT. The VAWT rotates clockwise when looking from top. The grey squares denote the projected frontal area of the VAWT [Colour figure can be viewed at wileyonlinelibrary.com]

is helpful in locating the strong CVPs. The green contour lines are plotted where $\bar{u}/U = 1$, representing the shape of the wake. The first row of Figure 10 depicts the initial topology of the streamwise vortical system in correspondence to the hypothesis, the second and the third rows show the development of the streamwise vorticity at $x/D = 3$ and 5 and the CVPs in the wake.

Due to the absence of the ground, the vorticity field is almost symmetrical with respect to $z/D = 0$, and the symmetry is slightly broken when the wake of tower starts to interact with the wake of the rotor, after $x/D = 5$. Based on the symmetry, only the upper halves of the wakes are marked in relation to the hypothesized vortical system. For all the cases, the hypothesized double-layer vorticity structures are clearly present initially at $x/D = 1$. The upper layers are generated in the downwind region of the rotor, while the lower layers are generated upwind. It is worth mentioning that there exists strong vorticity near $y/D = 0 \sim 0.5$ and $z/D = -0.25 \sim 0.25$, in the wake of P-10 at $x/D = 1$, as illustrated in Figure 10. This is due to a concentration of vorticity on the blades causing vortex roll-up. Apart from that, the propagating and merging of the vorticity field still follow the proposed model. However, further investigations are required if details such as vortex rolling-up and stretching need to be modelled.

The strong counter-rotating vortices are identified based on the in-plane streamlines. The cross-sections at $x/D = 3$ and 5 provide a cleaner view of the CVPs because the merging of the vortices occurs and only strong CVPs are left. The merging process is as follows: The smaller vortices will change their directions of rotation under the effect of the stronger vortex and then merge with the latter into a larger region with a weaker vorticity. For all the cases, the double-layer structure starts to break at $x/D = 3$ and disappears at $x/D = 5$.

P-10 features four pairs of CVPs in the wake, and its vorticity system is a combination of pattern (A) and (B) in Figure 3. The CVP-A$_a$ is slightly stronger than the CVP-B$_a$, resulting in a slight deflection to negative y. The CVP-A$_b$ and CVP-B$_b$ are responsible for the vertical expansion of the wake.
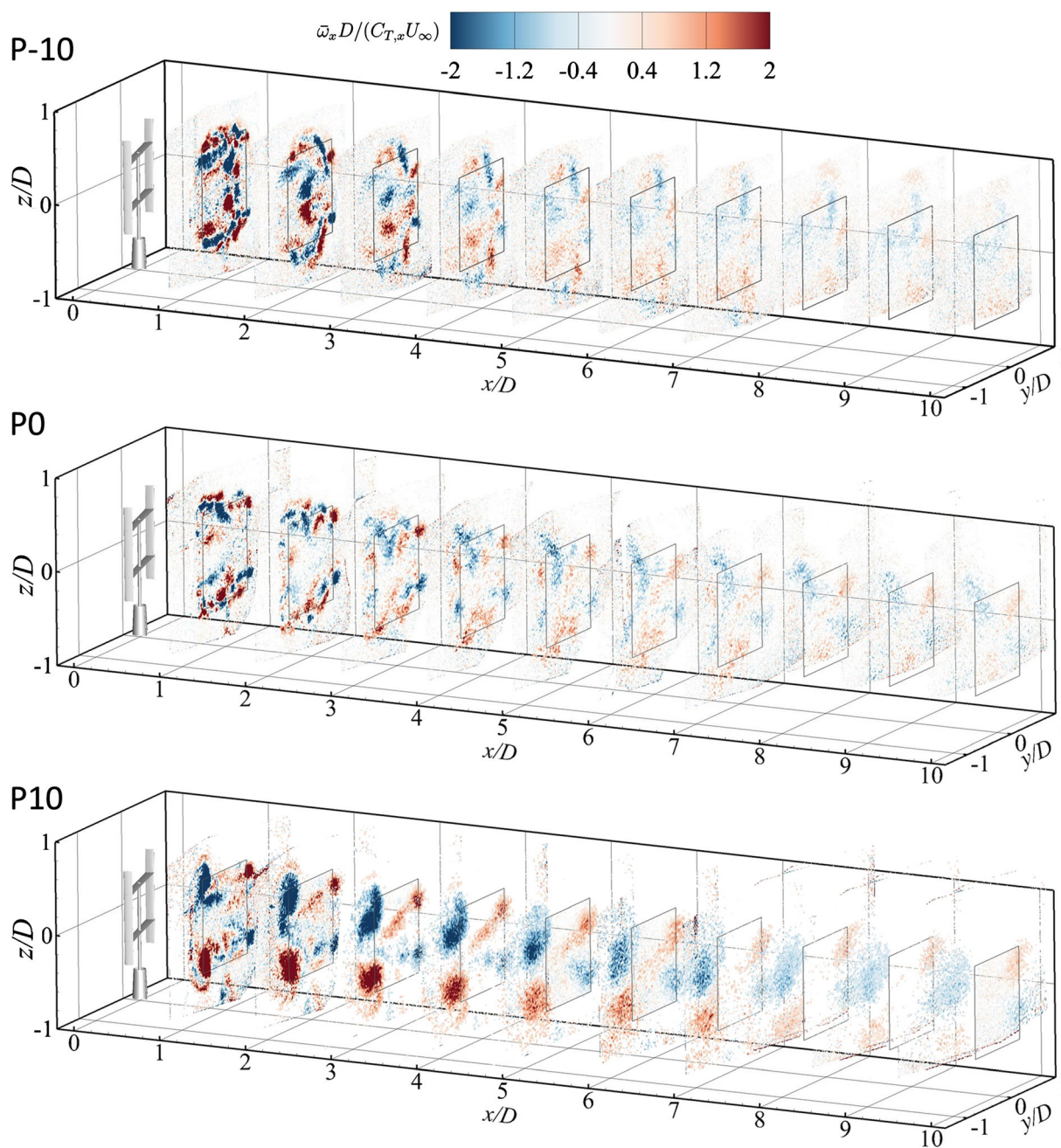
FIGURE 9 Contours of time-averaged normalized streamwise vorticity. The centre of the rotor is placed at the origin; grey squares in the successive cross-sections denote the projection of the frontal areal of the VAWT [Colour figure can be viewed at wileyonlinelibrary.com]

The vorticity system of P0 and P10 can be described with an asymmetrical version of pattern (A). In both cases, the CVP-A induces a larger transverse velocity to the windward side and thus results in a wake deflection. The distinct differences are (1) the location of the CVP-A: in the wake of P0, the CVP-A is located around the centreline of the rotor ($y/D = 0$), whereas the one in P10 is located around the edge of the wake at the windward side; (2) the strengths of the CVPs: in P10, the CVPs are so strong that merging of streamwise vortices occurs significantly. The CVPs entrain other streamwise vortices and merges them into larger regions much faster than P-10 and P0: At $x/D = 3$, the trace of weaker vortices is almost gone in the wake of P10. These differences are responsible for the distinctions in the wake deflection and deformation.

Additionally, the vorticity generated due to the presence of the struts is marked with capital S. This vorticity has a small effect on the wake deformation, which can be appreciated in the wake of P0 at $x/D = 5$.
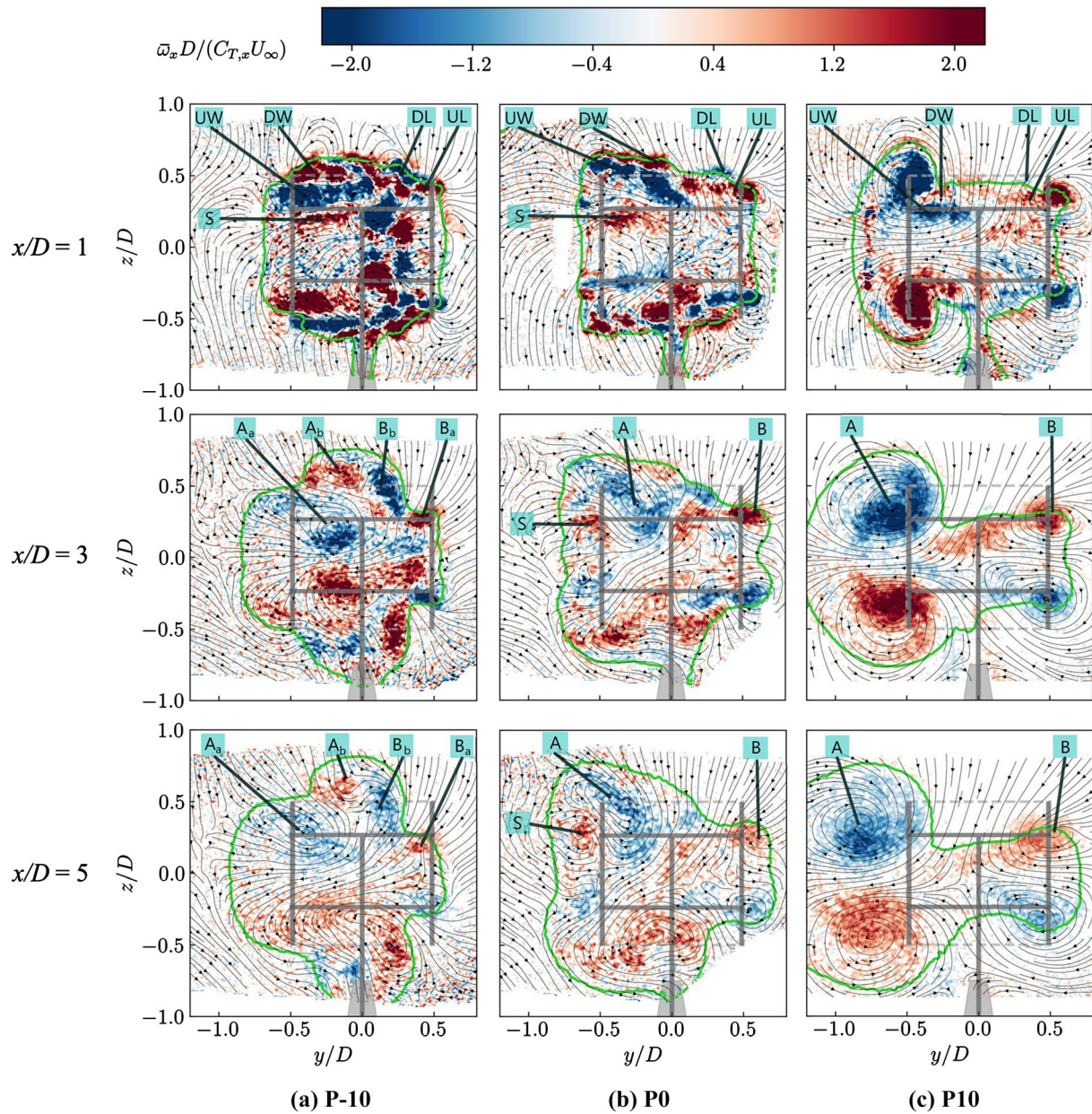
FIGURE 10 Contours of streamwise vorticity with in-plane streamlines for P-10, P0 and P10 at $x/D = 1,3,5$. The generation regions of the vorticity are marked corresponding to those in Figure 2. Green contour lines: $\bar{u}/U = 1$; A and B: the strong vortices at windward side and leeward side; S: the vorticity generated due to the presence of the struts [Colour figure can be viewed at wileyonlinelibrary.com]

3.5 | Turbulence Intensity

The TI magnitude $I_{|U|} = \sqrt{\overline{u'u'} + \overline{v'v'} + \overline{w'w'}}/U$, is illustrated in Figure 11. For all the cases, $I_{|U|}$ is mostly concentrated at the interface between the freestream and the wake, that is, the perimeter of the wake cross-section. As indicated in the previous study from Huang et al,[40] the longer the perimeter, the faster momentum recovery due to the turbulent diffusion and shear is expected, provided that the overall streamwise thrust is the same.

The TI fields correlate well with the vorticity fields, with high $I_{|U|}$ in regions of strong vorticity. In P-10, the maximum TI concentrates around the centre right of the wake, which is also the region of the standing out CVPs discussed in Section 3.4. P0 and P10 feature the same pattern, with the maximum $I_{|U|}$ at the spots of the CVPs. Besides that, the $I_{|U|}$ contours depict the shape of the wake perimeter.
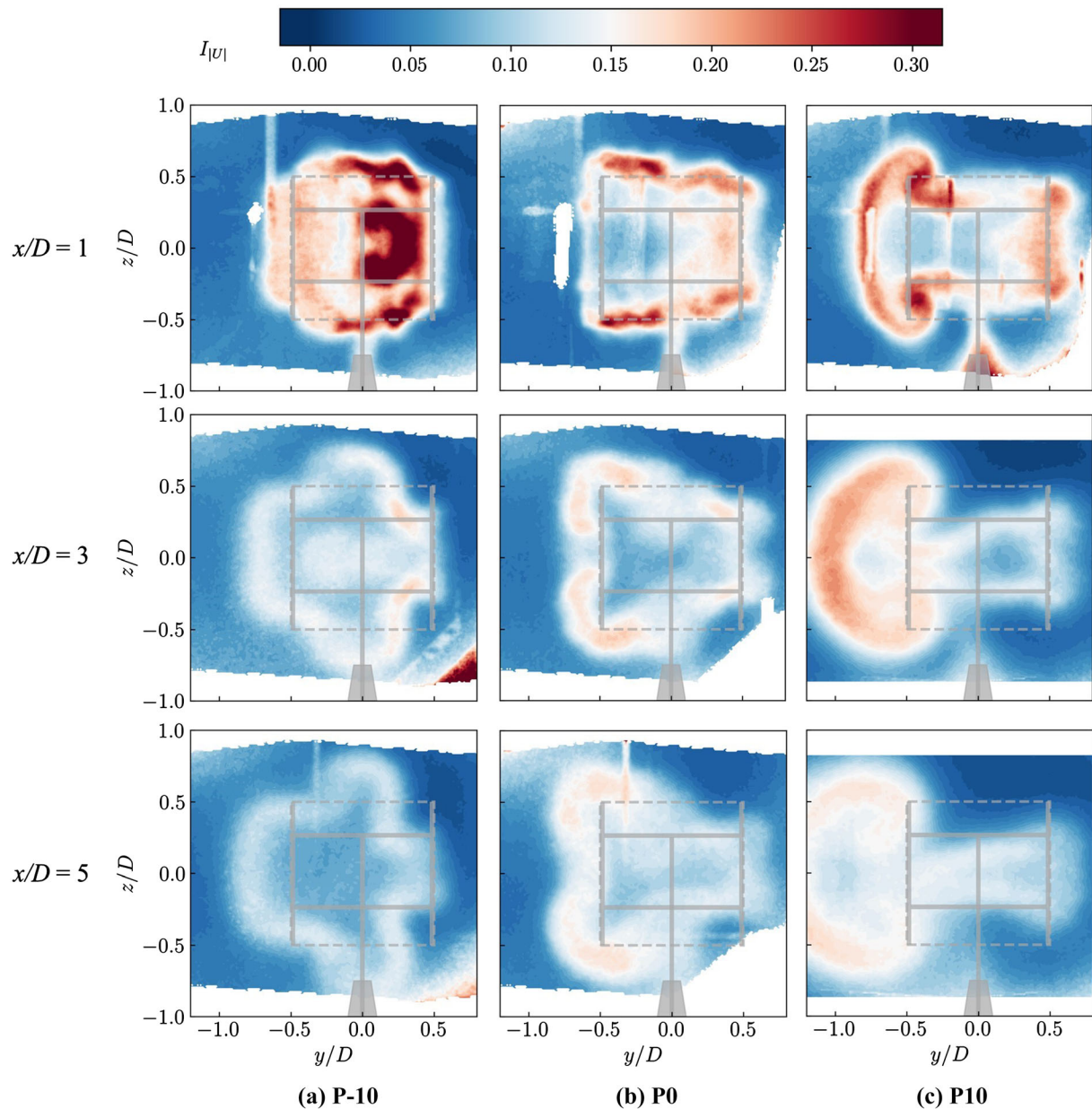
FIGURE 11 Contours of turbulence intensity magnitudes, $I_{|U|}$, for P-10, P0 and P10 at $x/D = 1,3,5$ [Colour figure can be viewed at wileyonlinelibrary.com]

4 | THE IMPACT OF PITCHED BLADES ON VAWT ARRAYS

4.1 | Velocity deficit and wake centre development

The distributions of streamwise velocity deficits $((\bar{u} - U)/U)$ for all the cases are compared in Figure 12, where the cross-sections at $x/D = 1,3,5$ are presented. From left to right are case P-10, P0 and P10, which generate deficit areas that feature shapes of octagon, trapezoid and left-arrow at $x/D = 1$, respectively. The maximum deficit of P-10 is shifted slightly to the right compared to P0; P10 shifts to the left largely, which is clearly attributed to the larger side force generated by the VAWT at positive pitch and hence to the strong counter-rotating vortices in the wake.

The in-plane velocity vectors disclose the trace of at least two pairs of streamwise CVPs, as discussed in Section 3.4. With the effects of these CVPs, the wake shapes are quickly deformed along the streamwise directions: Those of P0 and P10 become thinner vertically at $y/D = 0$, whereas the wake of P-10 expands remarkably along the spanwise direction z.
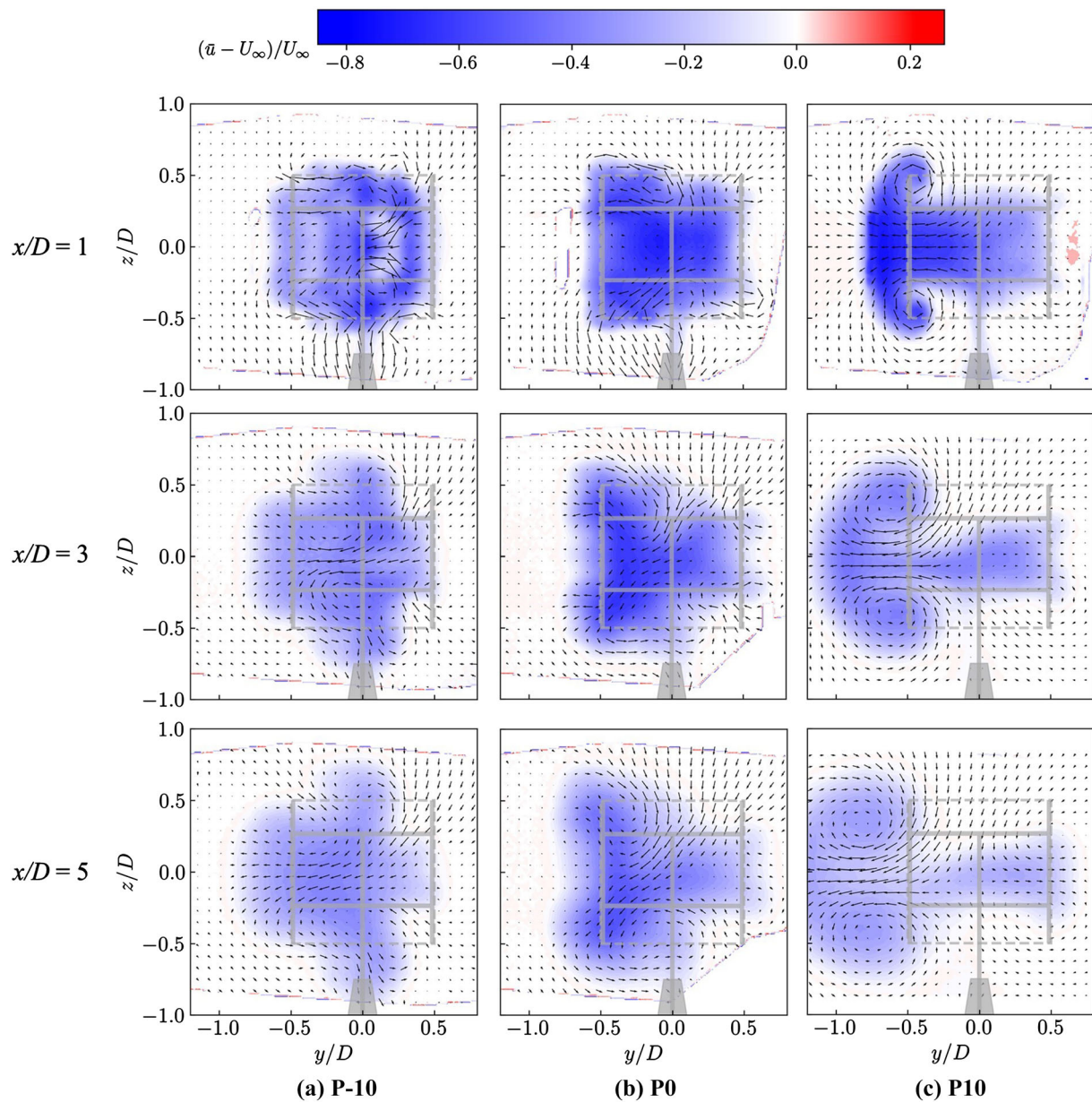
FIGURE 12 Contours of velocity deficit with in-plane velocity vectors for case P-10, P0 and P10, at $x/D = 1,3,5$. Schematics for the VAWT with tower are marked in grey [Colour figure can be viewed at wileyonlinelibrary.com]

The wake centre developments are compared in Figure 13. As expected, the positive pitch produces the largest deflection towards the windward side (negative y), which is nearly twice that of the P0 case; instead, the wake deflections of the P0 and P-10 cases are very similar, with the negative pitch yielding slightly larger deflection after $x/D = 5$. All the cases feature approximately linear wake deflections within near wake (5D), which is also observed in the wake of HAWTs with a constant yaw angle.[51] It is noted that the wake shapes of VAWTs are complex and the calculation of wake centre may not be the optimal approach to quantify the wake deflection. In the far wake, the deflection should eventually reach an asymptotic value.

4.2 | Streamwise momentum recovery

The available terms of Equation (9) are calculated at $x/D = 3$ and depicted in contour plots in Figure 14. The pressure term is not measured, therefore is omitted in the comparison. The in-plane spatial derivative $\partial/\partial y$ and $\partial/\partial z$ are calculated with second order central difference within the measured cross-sections. Due to the relatively large separation between the cross-flow planes, it is not possible to accurately evaluate the
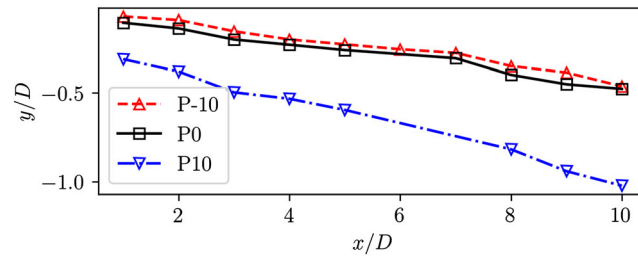
FIGURE 13 Comparison of the lateral deflections of the wake centre for varying streamwise distance from the turbine [Colour figure can be viewed at wileyonlinelibrary.com]
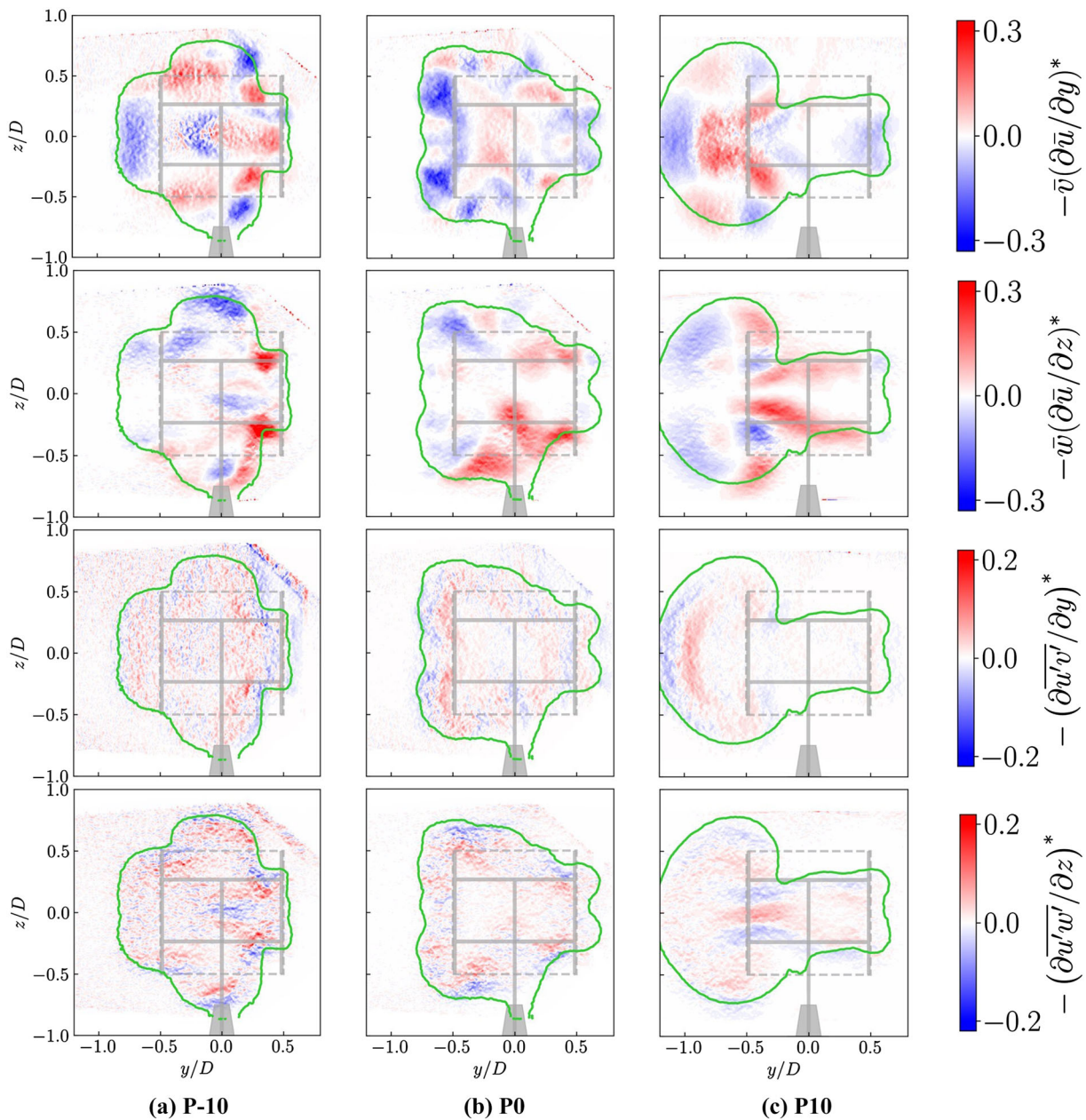

FIGURE 14 Measured terms of the RANS equation in the streamwise direction. For each case, the terms are normalized by the maximum value of $\bar{u}(\partial\bar{u}/\partial x)$, as denoted by * [Colour figure can be viewed at wileyonlinelibrary.com]

streamwise derivatives $\partial/\partial x$, and therefore, the related terms ($\bar{u}(\partial\bar{u}/\partial x)$ and $\partial\overline{u'u'}/\partial x$) are not presented. However, $\partial\bar{u}/\partial x$ is calculated using second order polynomial regression with the data at $x/D = 2$ and 4, to get an evaluation of the maximum value of $\bar{u}(\partial\bar{u}/\partial x)$ for each case, as the normalization values for the presented terms in Figure 14, following the work of Bossuyt et al. (2021).[19] In this way, one can identify the main contributors to the redistribution of the streamwise momentum in the wake, based on a relative comparison of the momentum budget.

In Figure 14, positive values contribute to the momentum recovery positively, and vice versa. The first row presents the horizontal advection of streamwise momentum. All three cases feature negative regions on the windward edges of the wakes due to substantial horizontal expansions that transport low momentum flow from the centre of the wake to the edges.

The vertical advection of streamwise momentum is illustrated at the second row. It is clear that for all these cases, the vertical advection contributes positively on the leeward side, where the heights of the wakes are shrinking due to the vorticity system discussed in Section 3.4. Such motion entrains high-momentum flow into the wake. On the contrary, the vertical advection contributes negatively where the vertical expansion of the wake occurs; the latter transport low momentum flow from the wake centre to the edges. For P-10, such expansion regions locate along the centre and the windward side of the wake, while P0 and P10 expand majorly at their windward edges.

Based on the visual comparisons between the two top rows and the two bottom rows of Figure 14, the advection of momentum plays a more critical role in redistributing the streamwise momentum than the Reynolds stress terms. This is attributed to the in-plane velocity vectors being relatively strong at $x/D = 3$.

Another important observation is that the distributions of transport of momentum both by the mean flow and the turbulence are affected by the wake shape, namely, the recovery concentrates along the perimeter of the cross-section of the wake. In comparison, P10 creates a more extended wake perimeter than P0, while P-10 makes a shorter one. To better understand the effect of the deformed wake on the wake recovery, the averaged budgets of the wake recovery rate are compared in Figure 15. The process follows the work of Boudreau and Dumas (2017),[36] with Equation (9) being rearranged as

$$\frac{\partial\bar{u}}{\partial x} = \frac{1}{\bar{u}}\left(-\bar{v}\frac{\partial\bar{u}}{\partial y} - \bar{w}\frac{\partial\bar{u}}{\partial z} - \frac{1}{\rho}\frac{\partial\bar{p}}{\partial x} - \frac{\partial\overline{u'u'}}{\partial x} - \frac{\partial\overline{u'v'}}{\partial y} - \frac{\partial\overline{u'w'}}{\partial z}\right). \tag{13}$$

As aforementioned, only the in-plane advection and Reynolds stress terms are examined, and they are normalized with U/D. It has to be clarified that, compared to the previous work of Boudreau and Dumas (2017),[36] the terms presented here are averaged within the wake region that is determined by the contour line of $\bar{u}/U = 1$, instead of a square region that is identical to the frontal area of the turbine, to account for the deformed cross-sectional shape of the wake.

With Figure 15, one can identify each term's net contribution to the momentum recovery within the wake. The horizontal advection (the first term) has minimal effect on the total momentum recovery for P-10; on the contrary, it costs quite a portion of momentum to redistribute the
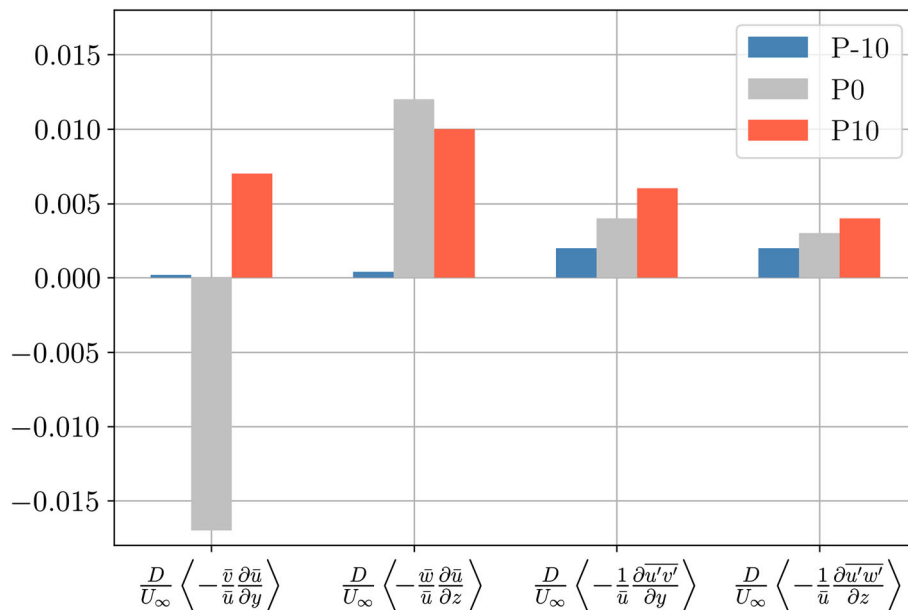

FIGURE 15 Budgets of the wake recovery rate for all three cases at $x/D = 3$. Each term has been averaged within the corresponding wake region that is determined by the contour line of $u/U = 1$ (as illustrated with green contour lines in Figure 14). Angle brackets denote the spatial average within the wake region [Colour figure can be viewed at wileyonlinelibrary.com]

wake in P0 (so that it has a negative value) and entrains momentum for P10. On the other hand, the vertical advection (the second term) still has a small effect on the wake of P-10, while it contributes positively to the wake of P0 and P10. For all the three cases, the Reynolds stress terms always have a positive contribution to the momentum recovery, and they are positively related to the TI that concentrates along the wake perimeter, as shown in Figure 11.

Based on the above discussion, it can be concluded that, by pitching the blades, the resulting vortex system deflects and deforms the wake. The deflections are effective in redistributing the momentum in the wake, while the deformations are essential in modifying the wake perimeter, thus affecting the momentum recovery.

4.3 | AP for hypothetical downwind turbines

The integration of AP is carried out at $x/D = 1,3,5,8$. As shown in Figure 16, the cases P-10 and P0 feature an overall similar wake effect in terms of the AP distribution. In contrast, the P10 case is much more effective in shifting the low-power flow to the windward side, negative y in this case. In the proximity of the upstream turbine ($1D$), the AP for all the cases is similar, due to an onset stage of the wake where the largely deformed wake structure has not been fully developed. For the P10 case, the wake deflects quickly: The minimum AP is located at $y/D = 0.5$ already at a downstream distance $x/D = 3$.

At $x/D = 3$ and $y/D = 0$, the AP in the wake of P10 reaches 0.61 of that in the free stream, compared to 0.41 and 0.32 for P-10 and P0, respectively. At $x/D = 5$, the AP of P10 increases to 0.74 at inline location; further downstream, the AP increases at a lower rate, reaching 0.77 at
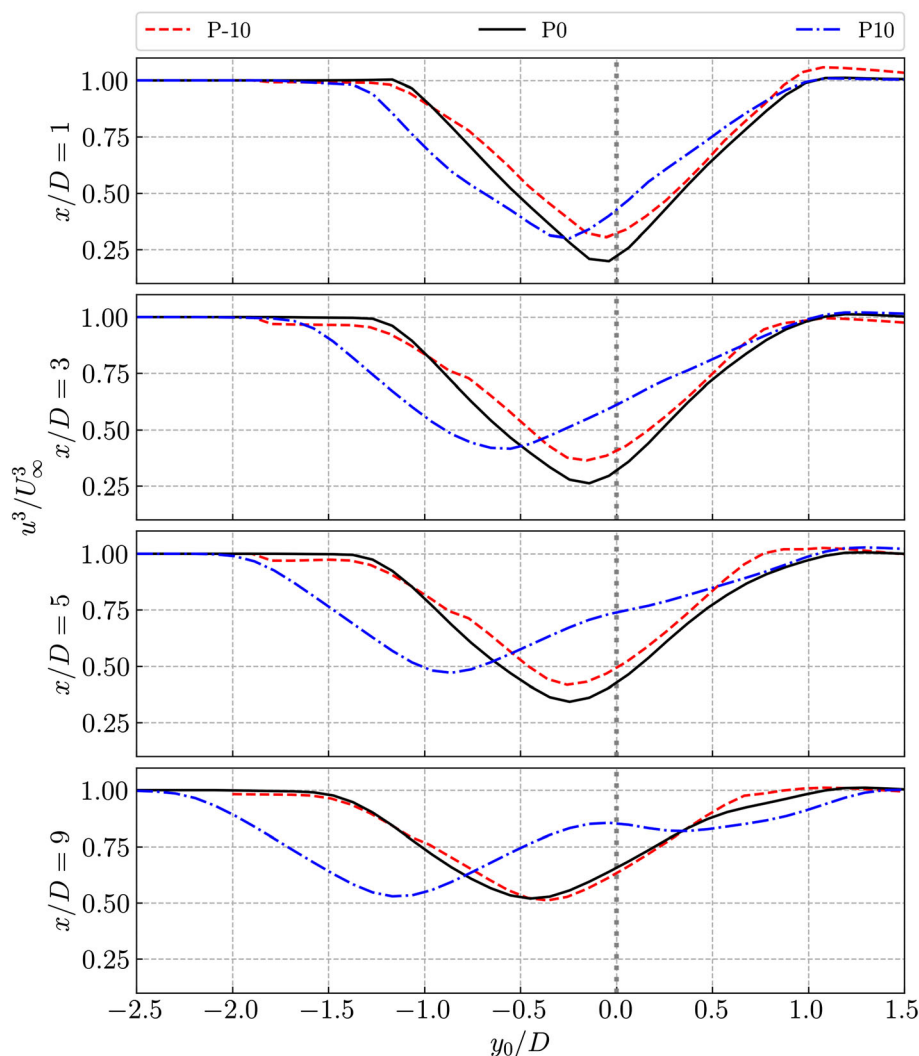

FIGURE 16 Available power distribution along transverse locations at $x/D = 1,3,5,8$ [Colour figure can be viewed at wileyonlinelibrary.com]

TABLE 5 Comparison of estimated AP using AD model, measured minimum AP and AP at $x/D = 1$ inline with the turbine

Case	$C_{T,x}$	$f_{AP|AD}$	$f_{AP|min,EXP}$	$f_{AP|inline,EXP}$			
				$x/D = 1$	$x/D = 3$	$x/D = 5$	$x/D = 8$
P-10	0.60	0.25	0.30	0.32	0.41	0.49	0.65
P0	0.65	0.21	0.19	0.22	0.32	0.43	0.63
P10	0.81	0.08	0.30	0.43	0.61	0.74	0.85

$x/D = 8$. The slow down of the increase of the AP occurs because the wake recovery at this location is no longer dominated by the advection of momentum, but by the turbulence transport and expansion, similarly to classical shear dominated turbulent wakes. Moreover, the transverse location of the minimum AP is constantly deflected to the windward side of the VAWT, yielding a shift exceeding $1D$ at $x/D = 8$.

A comparison of the measured AP coefficient with the estimated value from the AD model is provided in Table 5. The measured data are selected close to the VAWT model ($x/D = 1$) where the wake deficit has not recovered much. The measured minimum AP indicates the effect of the fixed blade pitch on the recovery of the wake. The baseline P0 features a great match with the theory, showing that the streamwise momentum conservation is valid for a regular VAWT; P-10 also shows a good agreement, with a slightly increase of the f_{AP} due to the recovery of the wake; conversely, the AP in the P10 case features a clear mismatch with the AD theory, because the latter cannot reproduce the wake deflection caused by the pitched the blades. The f_{AP} is increased by nearly 300% compared to the prediction, which is due to the enhancement of the momentum advection that follows the large streamwise vortical structure introduced in Section 3.3 and discussed in more details in Section 3.4. On the other hand, the comparison of f_{AP} at inline location ($x/D = 1, y/D = 0$) proves the effectiveness of P10: Even with a higher $C_{T,x}$ of the upwind turbine, the AP increases by nearly 100% compared to the P0 case. Conversely, P-10 has little improvement considering the less loaded rotor; in other terms, the increase of AP for P-10 is mostly the effect of a lower $C_{T,x}$.

5 | CONCLUSIONS

The effect of VAWTs' load distribution on its wake deflection is theoretically investigated using the AC model with an infinite-blade assumption. The proposed vortical structure is further validated using stereoscopic PIV measurements of the wake deflection caused by changing the fixed blade-pitch of a VAWT. The measured velocity, vorticity and turbulence fields are used to illustrate the pitched blade effect and to explain the physics of wake structure formation.

This work emphasises the importance of the streamwise vortical system. The streamwise vortices in the wake, generated at the top and bottom of the rotor as a consequence of the VAWT loading, are the main driver of the wake deflection and deformation.

The distribution of TI follows the wake's topology, with the majority of $I_{|U|}$ concentrated along the wake's perimeter. By examining the streamwise momentum budgets in the RANS equation, it is found that the momentum recovery within the VAWT wake is primarily due to the momentum advection along the wake perimeter, whereas the turbulence transport plays a less relevant role.

The VAWT with positively pitched blades (case P10) exhibits the greatest wake deflection, resulting in the highest AP for a hypothetical downwind turbine aligned with the upwind turbine, while P0 and P-10 (0 and -10 degrees pitch) exhibit wake deflections that are comparable between them and significantly lower than the P10 case.

CONFLICT OF INTEREST

The authors report no conflict of interest.

PEER REVIEW

The peer review history for this article is available at https://publons.com/publon/10.1002/we.2803.

DATA AVAILABILITY STATEMENT

The data that support the findings of this study are openly available in the 4TU repository at https://doi.org/10.4121/14685978.

ORCID

Ming Huang 🄳 https://orcid.org/0000-0003-3942-3871

REFERENCES

1. Porté-Agel F, Bastankhah M, Shamsoddin S. Wind-turbine and wind-farm flows: a review. *Bound-Layer Meteorol*. 2020;174(1):1-59.
2. Fleming P, Annoni J, Shah JJ, et al. Field test of wake steering at an offshore wind farm. *Wind Energy Sci*. 2017;2:229-239. https://www.wind-energ-sci.net/2/229/2017/
3. Fleming P, King J, Dykes K, et al. Initial results from a field campaign of wake steering applied at a commercial wind farm—part 1. *Wind Energy Sci*. 2019;4(2):273-285.
4. Park J, Law KH. Cooperative wind turbine control for maximizing wind farm power using sequential convex programming. *Energy Conv Manag*. 2015; 101:295-316.
5. Boersma S, Doekemeijer BM, Gebraad PMO, et al. A tutorial on control-oriented modeling and control of wind farms. In: Proceedings of the American Control Conference. IEEE; 2017:1-18.
6. Bastankhah M, Porté-Agel F. Wind farm power optimization via yaw angle control: a wind tunnel study. *J Renew Sustain Energy*. 2019;11(2):23301. https://aip-scitation-org.tudelft.idm.oclc.org/doi/abs/10.1063/1.5077038
7. Howland MF, Lele SK, Dabiri JO. Wind farm power optimization through wake steering. *Proc Nat Acad Sci United States America*. 2019;116(29): 14495-14500.
8. Parkin P, Holm R, Medici D. The application of PIV to the wake of a wind turbine in yaw. In: *Proc. 4th International Symposium on Particle Image Velocimetry. Göttingen, Germany*; 2001.
9. Medici D, Alfredsson PH. Measurements on a wind turbine wake: 3D effects and bluff body vortex shedding. *Wind Energy*. 2006;9(3):219-236. https://onlinelibrary-wiley-com.tudelft.idm.oclc.org/doi/10.1002/we.156
10. Bartl J, Mühle F, Schottler J, et al. Wind tunnel experiments on wind turbine wakes in yaw: effects of inflow turbulence and shear. *Wind Energy Sci*. 2018;3(1):329-343.
11. Jiménez A, Crespo A, Migoya E. Application of a LES technique to characterize the wake deflection of a wind turbine in yaw. *Wind Energy*. 2010;13(6): 559-572. https://onlinelibrary-wiley-com.tudelft.idm.oclc.org/doi/10.1002/we.380
12. Shapiro CR, Gayme DF, Meneveau C. Modelling yawed wind turbine wakes: a lifting line approach. *J Fluid Mech*. 2018;841:R11-R112.
13. Bastankhah M, Porté-Agel F. Experimental and theoretical study of wind turbine wakes in yawed conditions. *J Fluid Mech*. 2016;806:506-541. http://www.journals.cambridge.org/abstract_S0022112016005954
14. Zong H, Porté-Agel F. A point vortex transportation model for yawed wind turbine wakes. *J Fluid Mech*. 2020;890:A8. https://www-cambridge-org. tudelft.idm.oclc.org/core/journals/journal-of-fluid-mechanics/article/point-vortex-transportation-model-for-yawed-wind-turbine-wakes/ BFFD4FB29ADE4E4A20133850DBC5EFB7
15. Fleming PA, Gebraad PMO, Lee S, et al. Evaluating techniques for redirecting turbine wakes using SOWFA. *Renew Energy*. 2014;70:211-218. https://doi.org/10.1016/j.renene.2014.02.015
16. Nanos EM, Letizia S, Clemente DJB, Wang C, Rotea M, Bottasso CL. Vertical wake deflection for offshore floating wind turbines by differential ballast control. *J Phys: Conf Ser*. 2020;1618:22047.
17. Stevens RJAM, Meneveau C. Flow structure and turbulence in wind farms. *Ann Rev Fluid Mech*. 2017;49:311-339. https://www.annualreviews.org
18. Hamilton N, Kang HS, Meneveau C, Cal RB. Statistical analysis of kinetic energy entrainment in a model wind turbine array boundary layer. *J Renew Sustain Energy*. 2012;4(6):63105. http://aip.scitation.org/doi/10.1063/1.4761921
19. Bossuyt J, Scott R, Ali N, Cal RB. Quantification of wake shape modulation and deflection for tilt and yaw misaligned wind turbines. *J Fluid Mech*. 2021;917:A3. https://www.cambridge.org/core/product/identifier/S0022112021002378/type/journal_article
20. Bastankhah M, Shapiro CR, Shamsoddin S, Gayme DF, Meneveau C. A vortex sheet based analytical model of the curled wake behind yawed wind turbines. *J Fluid Mech*. 2021;933:A2. https://doi.org/10.1017/jfm.2021.1010
21. Campagnolo F, Petrović V, Bottasso CL, Croce A. Wind tunnel testing of wake control strategies. In: Proceedings of the American Control Conference. Institute of Electrical and Electronics Engineers Inc.; 2016:513-518.
22. Meyers J, Meneveau C. Optimal turbine spacing in fully developed wind farm boundary layers. *Wind Energy*. 2012;15(2):305-317. https://onlinelibrary-wiley-com.tudelft.idm.oclc.org/doi/10.1002/we.469
23. Stevens RJAM, Gayme DF, Meneveau C. Effects of turbine spacing on the power output of extended wind-farms. *Wind Energy*. 2016;19:359-370.
24. Stevens RJAM, Gayme DF, Meneveau C. Large eddy simulation studies of the effects of alignment and wind farm length. *J Renew Sustain Energy*. 2014;6(2):23105. https://aip-scitation-org.tudelft.idm.oclc.org/doi/abs/10.1063/1.4869568
25. Rolin VFC, Porté-Agel F. Experimental investigation of vertical-axis wind-turbine wakes in boundary layer flow. *Renew Energy*. 2018;118:1-13.
26. Chatelain P, Duponcheel M, Zeoli S, et al. Investigation of the effect of inflow turbulence on vertical axis wind turbine wakes. *J Phys: Conf Ser*. 2017; 854:12011. https://iopscience.iop.org/article/10.1088/1742-6596/854/1/012011/meta
27. Hezaveh SH, Bou-Zeid E, Dabiri J, Kinzel M, Cortina G, Martinelli L. Increasing the power production of vertical-axis wind-turbine farms using synergistic clustering. *Bound-Layer Meteorol*. 2018;169(2):1-22. https://doi.org/10.1007/s10546-018-0368-0
28. Jadeja A. Wake Deflection Technique for Vertical Axis Wind Turbines using Actuator Line Model in OpenFOAM. *Master's Thesis*: Delft University of Technology; 2018.
29. Guo J, Lei L. Flow characteristics of a straight-bladed vertical axis wind turbine with inclined pitch axes. *Energies*. 2020;13(23):6281. https://www. mdpi.com/1996-1073/13/23/6281
30. Mendoza V, Goude A. Improving farm efficiency of interacting vertical-axis wind turbines through wake deflection using pitched struts. *Wind Energy*. 2019;22(4):538-546. https://onlinelibrary.wiley.com/doi/abs/10.1002/we.2305
31. Wei NJ, Brownstein ID, Cardona JL, Howland MF, Dabiri JO. Near-wake structure of full-scale vertical-axis wind turbines. *J Fluid Mech*. 2021;914:17. https://doi.org/10.1017/jfm.2020.578
32. Buchner AJ, Soria J, Honnery D, Smits AJ. Dynamic stall in vertical axis wind turbines: scaling and topological considerations. *J Fluid Mech*. 2020;841: 746-766. https://doi.org/10.1017/jfm.2018.112

33. Ryan KJ, Coletti F, Elkins CJ, Dabiri JO, Eaton JK. Three-dimensional flow field around and downstream of a subscale model rotating vertical axis wind turbine. *Experiments Fluids*. 2016;57(3):38. http://link.springer.com/10.1007/s00348-016-2122-z

34. Tescione G, Ragni D, He C, Simão Ferreira CJ, van Bussel GJW. Near wake flow analysis of a vertical axis wind turbine by stereoscopic particle image velocimetry. *Renew Energy*. 2014;70:47-61.

35. Ouro P, Runge S, Luo Q, Stoesser T. Three-dimensionality of the wake recovery behind a vertical axis turbine. *Renew Energy*. 2019;133:1066-1077. https://doi.org/10.1016/j.renene.2018.10.111

36. Boudreau M, Dumas G. Comparison of the wake recovery of the axial-flow and cross-flow turbine concepts. *J Wind Eng Industr Aerodyn*. 2017;165: 137-152.

37. Araya DB, Colonius T, Dabiri JO. Transition to bluff-body dynamics in the wake of vertical-axis wind turbines. *J Fluid Mech*. 2017;813:346-381.

38. Craig AE, Dabiri JO, Koseff JR. Flow kinematics in variable-height rotating cylinder arrays. *J Fluids Eng*. 2016;138(11):111203. http://fluidsengineering.asmedigitalcollection.asme.org/article.aspx?doi=10.1115/1.4033676

39. Craig AE, Dabiri JO, Koseff JR. Low order physical models of vertical axis wind turbines. *J Renew Sustain Energy*. 2017;9(1):1-17. http://aip.scitation.org/doi/10.1063/1.4976983

40. Huang M, Ferreira C, Sciacchitano A, Scarano F. Experimental comparison of the wake of a vertical axis wind turbine and planar actuator surfaces. *J Phys: Conf Ser*. 2020;1618(5):52063.

41. De Tavernier D, Ferreira C, Paulsen U, Madsen H. The 3D effects of a vertical-axis wind turbine: rotor and wake induction. *J Phys: Conf Ser*. 2020; 1618:52040.

42. Massie L, Ouro P, Stoesser T, Luo Q. An actuator surface model to simulate vertical axis turbines. *Energies*. 2019;12(24):1-16.

43. Ferreira C. The Near Wake of the VAWT 2D and 3D Views of the VAWT Aerodynamics. *Ph.D. Thesis*: Delft University of Technology; 2009.

44. LeBlanc B, Ferreira C. Estimation of blade loads for a variable pitch vertical axis wind turbine from particle image velocimetry. *Wind Energy*. 2022; 25(2):313-332.

45. Anderson JD. *Fundamentals of Aerodynamics*. 5th ed.: McGraw-Hill; 2011. http://www.worldcat.org/isbn/9780073398105

46. Madsen HA, Paulsen US, Vitae L. Analysis of VAWT aerodynamics and design using the actuator cylinder flow model. *J Phys: Conf Ser*. 2014;555(1): 12065.

47. Leblanc B, Ferreira C. Experimental demonstration of thrust vectoring with a vertical axis wind turbine using normal load measurements. *J Phys: Conf Ser*. 2020;1618(5):52030. https://iopscience-iop-org.tudelft.idm.oclc.org/article/10.1088/1742-6596/1618/5/052030/meta

48. Lignarolo LEM, Ragni D, Scarano F, Simão Ferreira CJ, Van Bussel GJW. Tip-vortex instability and turbulent mixing in wind-turbine wakes. *J Fluid Mech*. 2015;781:467-493. https://doi.org/10.1017/jfm.2015.470

49. Sciacchitano A, Wieneke B. PIV uncertainty propagation. *Measurement Sci Technol*. 2016;27(8):84006. https://iopscience-iop-org.tudelft.idm.oclc.org/article/10.1088/0957-0233/27/8/084006/meta

50. Madsen HA. On the ideal and real energy conversion in a straight bladed vertical axis wind turbine. Tech. Rep., The Institute of Industrial Constructions and Energy Technology, Aalborg University Centre; 1983.

51. Howland MF, Bossuyt J, Martínez-Tossas LA, Meyers J, Meneveau C. Wake structure in actuator disk models of wind turbines in yaw under uniform inflow conditions. *J Renew Sustain Energy*. 2016;8:43301.

52. Devenport WJ, Rife MC, Liapis SI, Follin GJ. The structure and development of a wing-tip vortex. *J Fluid Mech*. 1996;312:67-106. https://doi.org/10.1017/S0022112096001929

APPENDIX A: THE PRINCIPLE OF VORTEX GENERATION BY FORCE FIELDS

Consider the Navier–Stokes equation for the conservation of momentum:

$$\rho\frac{D\mathbf{U}}{Dt} = \mathbf{f} - \nabla p + \mu\nabla^2\mathbf{U}, \tag{A1}$$

where $\mathbf{f}$, p, $\mathbf{U}$ and μ are the body force, pressure, velocity and dynamic viscosity, respectively. The bold letters represent vectors.

Taking the curl of Equation (A1), the vorticity transport equation is obtained:

$$\rho\frac{D\boldsymbol{\omega}}{Dt} = \nabla\times\mathbf{f} + (\boldsymbol{\omega}\cdot\nabla)\mathbf{U} - \boldsymbol{\omega}(\nabla\cdot\mathbf{U}) + \mu\nabla^2\boldsymbol{\omega}, \tag{A2}$$

where $\boldsymbol{\omega}$ is the vorticity vector: $\boldsymbol{\omega} = \nabla\times\mathbf{U}$. Because a flow field wherein a wind turbine is placed can be regarded as incompressible, the third term in the RHS is zero. The viscous term $\mu\nabla^2\boldsymbol{\omega}$ can be neglected due to a sufficiently large Reynolds number. For a uniform inflow that is irrational originally, the term $(\boldsymbol{\omega}\cdot\nabla)\mathbf{U}$ will remain zero until vorticity is generated by the curl of a force field. Therefore, it is clear that the generation of
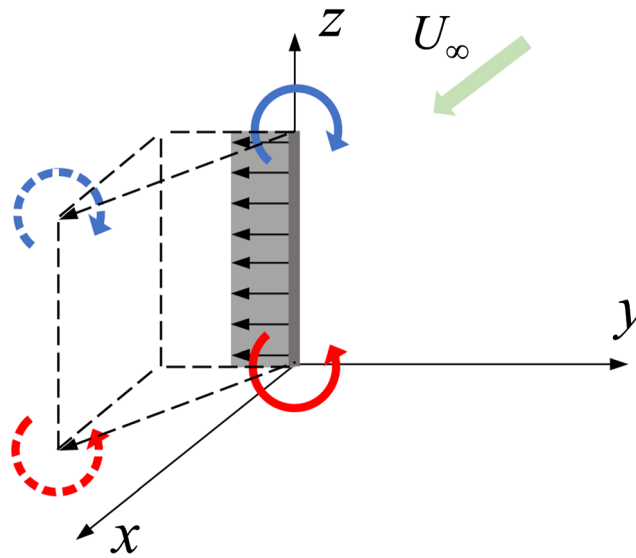
FIGURE A1   A schematic of the vortex generated by an actuator line in the 3D space [Colour figure can be viewed at wileyonlinelibrary.com]

vorticity is attributed to a specific force field. To demonstrate the vortex generation principle, assume a uniform force field **f** that is distributed on a line element placed along the z-axis in a 3D space, as depicted in Figure A1; the latter is usually referred to as an actuator line (AL). The AL applies a force to the flow towards the direction of negative y. The incoming flow U is directed towards the positive x. Applying Equation (A2) to the AL, the material derivative of the vorticity vector is given by

$$\rho\frac{D\boldsymbol{\omega}}{Dt} = \nabla \times \mathbf{f} = \left(\frac{\partial f_z}{\partial y} - \frac{\partial f_y}{\partial z}\right)\hat{i} + \left(\frac{\partial f_x}{\partial z} - \frac{\partial f_z}{\partial x}\right)\hat{j} + \left(\frac{\partial f_y}{\partial x} - \frac{\partial f_x}{\partial y}\right)\hat{k} = -\frac{\partial f_y}{\partial z}\hat{i},$$ (A3)

where $\hat{i}, \hat{j}$ and $\hat{k}$ are the unit vectors for the x, y and z axes, respectively. According to Equation (A3), vorticity is generated only when the spatial gradient of a force field is not null, that is, at the extremities of the actuator line. For a simple uniform AL as illustrated, a pair of counter-rotating vortices are thus generated, whose axis is perpendicular to the plane defined by the force vector and the actuator line. The counter-rotating vortices propagate along the free-stream direction (positive x), they are also deflected laterally (towards negative y) under the effect of the transverse velocity induced by the force field. It should be noted that in the above discussion the stretching and redirecting of the vortices are omitted for sake of simplicity, and this simplification is valid in the near wake of the AL. A similar phenomenon occurs in the wakes of airplanes, whereby the lift distribution over the wing generates a pair of counter-rotating tip vortices which move downwards under the effect of the downwash they induce.[52]